AIMS Bioengineering

http://www.aimspress.com/journal/Bioengineering

AIMS Bioengineering, 9(1): 44–60.
DOI: 10.3934/bioeng.2022004
Received: 12 December 2022
Revised: 23 January 2022
Accepted: 25 January 2022
Published: 07 February 2022

Research article

Multicellular model of angiogenesis

Takashi Nakazawa[1], Sohei Tasaki[2], Kiyohiko Nakai[3] and Takashi Suzuki[1,*]

[1] Center for Mathematical Modelling and Data Science, Osaka University, 1-3, Machikaneyama-cho, Toyonaka-shi, Osaka 560-8531, Japan

[2] Department of Mathematics, Faculty of Science, Hokkaido University, Kita-10, Nishi-8, Kita-ku, Sapporo 060-0810, Japan

[3] Chugai Pharmaceutical Co. Ltd., 2-1-1 Nihonbashi-Muromachi, Chuo-ku, Tokyo 103-8324, Japan

* **Correspondence:** Email: suzuki@sigmath.es.osaka-u.ac.jp; Tel: +810668506475.

Abstract: This paper presents a mathematical model governing the dynamics of a morphogenetic vascular endothelial cell (EC) during angiogenesis, and vascular growth formed by EC. Especially, we adopt a multiparticle system for modeling these cells. This model does not distinguish a tip cell from a stalk cell. A formed vessel is modeled using phase-field equation to prevent capillary expansion with time stepping in particular. Numerical simulation reveals that all cells are moving in the direction of high concentration of vascular endothelial growth factor (VEGF), and that they are mutually repellent in cases in which they are closer than some threshold.

Keywords: angiogenesis; multi-agent model; reaction–diffusion equation; finite element method

1. Introduction

Angiogenesis is a multicellular phenomenon by which new blood vessels emerge from an existing vascular system. Especially, tip cell selection plays an important role not only for lateral inhibitation but also for elongation, branching, anastomosis, vessel stabilization, lumen formation, and so on [1, 2]. These events have elucidated the roles of endothelial cell (EC) signaling with the vascular endothelial growth factor (VEGF)-receptor, angiopoitin-Tie2 and Eprin–Eph pathways [1, 3, 4]. Moreover, it has been increasingly clarified that interaction between ECs and mural cells, including vascular smooth muscle cells and pericytes, has been implicated in the maintenance of the angiogenic process for appropriate organization [3–7].

In fact, mathematical modeling for vascular growth has attracted considerable interest in the last few years along with elucidation of the mechanisms of development and proliferative and quiescent features, not only of normal cells but also of tumor cells. As a result, an enormous number of phenomena in

biochemistry can be subject to mathematical modeling, such as proteins, capillaries, and tumors. Prime examples include the work of Frieboes et al., who coupled phase fields to discrete tumor growth with discrete random walks to model angiogenesis [8–10]. Also, Lima et al. [11] proposed the ten-species model. Perfahl et al. [12] considered multiscale modeling of vascular tumor growth.

Cellular automata can be a type of mathematical model that is useful for simulating systems and diseases at the cellular level. Features of cellular automata are simple and discrete systems in which a limited number of states are defined for one cell. Cellular automata can generate complicated behavior based on simple and local rules that determine the states of cells and neighboring cells, whereas distant cells exert no influence [13]. To date, using cellular automata, many models have been presented to elucidate cancer behavior, especially tumor growth and its effective factors [12, 14–16]. Competition for nutrients among normal and cancerous cells has been analyzed, as has the influence of the immune system response on tumor growth, as described in an earlier study [17].

Despite the numerous earlier studies, how the spatiotemporal regulation of molecules affects morphogenetic cell movement, and what type of cell collective/cell movement is involved in angiogenesis have remained elusive, largely because of the lack of a stable methodology for visualizing and assessing EC movement during angiogenesis. To clarify the relation between individual cell movements and angiogenesis morphology, and to dissect the underlying molecular and cellular mechanisms, Arima et al. [18] first established a system in which dynamic cell behavior is visualized using time-lapse microscopy. They set out to identify patterns of cellular behavior in an angiogenesis model through computational data processing. As a result, cell movements were quite dynamic. The ECs moved while changing their mutual relative positions at the tip in elongating branches. On the other hand, Takubo et al. [19] analyzed EC behaviours in an $in-vitro$ angiogenic sprouting assay using mouse aortic explants in combination with mathematical modelling. From an experimentally validated mathematical model, cohesive movements with anisotropic cell-to-cell interactions charactarized the EC motolity, which may drive branch elongation depending on a constant cell supply.

In light of the findings described above, we suggest a multilevel model to simulate dynamic cell movement affected by VEGF. Particularly, a multi-agent model is applied to describe cell movement. Some particles with a position vector and polarity mutually interact constantly, with effects of chemotaxis deriving from VEGF. Such cell movement leads to blood vessel formation based on a phase–field equation. The Cahn–Hilliard type, a representative fourth-order partial differential equation, is adopted. As described herein, both mathematical models are coupled to simulate angiogenesis. Then an arbitrary numerical scheme is prepared.

Thermodynamically consistent phase field models refer to a class of models satisfying the second law of thermodynamics. These models have been used for modeling numerous non-equilibrium multi-phase thermodynamical processes ranging from material science and fluid science to life sciences. For this study, we specifically examined a phase field model for time-dependent dynamic of binary material systems in which A is represented by a phase variable at $\phi = 1$ and phase B at $\phi = 0$. We chose the phase variable $\phi \in [0,1]$ with ϕ identified at the volume fraction of material A and $1-\phi$ the volume fraction of material B. The interface between the two phases, known as the transition layer between the two phases in the phase field model, is given as $0 < \phi < 1$. The interface is defined mathematically at $\phi = \frac{1}{2}$.

The Cahn-Hilliard, introduced by J. Cahn and J. Hilliard in [20] to describe processes of phase

separation, includes components of a binary fluid separated and forming pure domains for each component. It can be interpreted as the H^{-1} gradient flow of the Cahn–Hilliard energy functional as

$$F(\phi) = \int_\Omega \left[\frac{\epsilon_1}{2} |\nabla \phi|^2 + f(\phi) \right] dx, \tag{1.1}$$

where ϵ_1 is a parameter expressing the strength of the conformational entropy. For immiscible binary materials, we chose the bulk energy density as a double well potential for this study

$$f(\phi) = \epsilon_2 \phi^2 (1-\phi)^2, \tag{1.2}$$

where ϵ_2 represents the strength of the bulk mixing free energy.

Such a Cahn–Hilliard equation is a typical fourth-order partial differential equation. It is very difficult to obtain a numerical solution stably. A structure-preserving scheme based on the discrete variational derivative method (DVDM) proposed by Furihata and Matsuo [21] has successfully calculated the Cahn–Hilliard equation stably. However, the discontinuous Galerkin method has also been used to trace an interface between material A and material B with high efficiency [22, 23]. Nevertheless, these numerical techniques involve quite cumbersome procedures. Often, we face difficulties in implementing these numerical schemes into our mathematical model with fourth-order partial differential equations. For the study described herein, we chose the Morley finite element method discussed in [24, 25]. The Morley element is implemented in Freefem++ [26] using numerical calculations.

This paper is organized as follows. Section 2 introduces a governing equation representing cell movement as a multi-agent system, with vessel development based on a phase-field model, particularly the Cahn–Hilliard equation. Numerical procedures used to calculate such a coupling model between multi-agent system and phase-field equation are presented in Section 3. Throughout the numerical calculations, numerical results are described in Section 4. Finally, Section 5 concludes this paper.

2. Problem formulation

In this section, we present some basic concepts related to the suggested mathematical multicellular model for angiogenesis. For these purposes, one must describe some mathematical notations.

One can let $\Omega \subset \mathbb{R}^d \, (d = 1,2,3)$ be a bounded domain, where a position vector is expressed as $\boldsymbol{x} \in \Omega$. Cells are located at a position vector $\boldsymbol{x}_i$ and more moving at a velocity vector (polarity) $\boldsymbol{q}_i$ at a time $0 < t \leq T$ for a positive constant T, where $0 < i \leq N_{cell}$ represents an index for distinguishing each cell. In fact, VEGF c attracts such cells to be closer. Consequently, a new blood vessel (capillary) is formed after each cell degenerates fibronectin f and passes. At the next section, a position vector $\boldsymbol{x}_i(t)$, a velocity vector (polarity) $\boldsymbol{q}_i(t)$, and a fibronectin concentration $f(t,\boldsymbol{x})$ are constructed under a given VEGF $c(t,\boldsymbol{x})$.

2.1. Governing equation

As discussed above, we suggest equations of three kinds for modeling a mathematical multicellular model for angiogenesis, position vector, polarity for cells, and the fibronectin concentration. Hereinafter, it is assumed that VEFG is given. Also, arbitrary parameters cell mobility a_1, repulsive force between cells and fibronectin a_2 for a position vector $\boldsymbol{x}_i$ and M_q, chemotaxis to VEGF concentration a_3, cell

alignment effect a_4, reference size of cell polarity q_0 for polarity $\boldsymbol{q}_i$ and square of transition area width of fibronectin phase variable D, mobility of fibronectin regions M, radius of influence of cells a_5, fibronectin enzyme μ for the fibronectin concentration f are prepared. Let Δt represent a time increment, with n and N respectively denoting a time step for a time $t = n\Delta t$ and a maximum times step for $T = N\Delta t$. These equations are expressed as described hereinafter.

2.1.1. Equation of cell motion

From the discussion presented in the section above, a governing equation of a position vector $\boldsymbol{x}_i$ with the index i distinguishing each cell at a time t, is defined as follows

$$\frac{d\boldsymbol{x}_i}{dt} = \varphi(f)\left\{\hat{\boldsymbol{q}}_i + \sum_{j\neq i, j=1}^{N_{cell}} g_1(r_{i,j})\frac{\boldsymbol{x}_j - \boldsymbol{x}_i}{r_{i,j}}\right\} - a_2\nabla f \text{ in } \Omega\times(0,T), \tag{2.1}$$

$$\boldsymbol{x}_i = \boldsymbol{x}_i^0 \text{ at } t = 0. \tag{2.2}$$

The first term on the right-hand side represents that a particle can move in a vessel for $f = 0$, and not outside of a vessel for $f = 1$, where $\varphi(f)$ is expressed as

$$\varphi(f) = a_1 \exp(-4f), \tag{2.3}$$

and where $\hat{\boldsymbol{q}}_i$ represents the unit vector of $\boldsymbol{q}_i$, expressed as

$$\hat{\boldsymbol{q}}_i = \frac{\boldsymbol{q}_i}{|\boldsymbol{q}_i|}. \tag{2.4}$$

The second term on the right-hand side depicts a collision: interaction between particles. Also, $r_{i,j}, g_1\left(r_{i,j}\right)$ studied in [19, 27] are a distance and a restitution coefficient between $\boldsymbol{x}_i$ and $\boldsymbol{x}_j$ as

$$r_{i,j} = |\boldsymbol{x}_j - \boldsymbol{x}_i|, \tag{2.5}$$

$$g_1\left(r_{i,j}\right) = \begin{cases} F_{rep}\frac{r_{i,j}-d_{core}}{d_{core}} & \text{if } r_{i,j} < d_{core} \\ 0 & \text{if } d_{core} \le r_{i,j} < d_{neutral} \\ F_{att}\frac{r_{i,j}-d_{neutral}}{d_{qdh}-d_{neutral}} & \text{if } d_{neutral} \le r_{i,j} < d_{adh} \\ F_{att}\frac{d_{reach}-r_{i,j}}{d_{reach}-d_{adh}} & \text{if } d_{adh} \le r_{i,j} < d_{reach} \\ 0 & \text{if } d_{reach} \le r_{i,j} \end{cases}. \tag{2.6}$$

The third term on the right-hand side describes that cells are reaching and bouncing on the vessel wall. Also, $\boldsymbol{x}_i^0$ is an initial condition of $\boldsymbol{x}_i$.

2.1.2. Polarity of cell

We present a governing equation of a polarity $\boldsymbol{q}_i$ with the index i at a time t, defined as

$$\frac{d\boldsymbol{q}_i}{dt} = M_q\left(q_0^2 - |\boldsymbol{q}_i|^2\right)\boldsymbol{q}_i + a_3\nabla c + \boldsymbol{\zeta}_i + a_4\frac{d\boldsymbol{x}_i}{dt} \text{ in } \Omega\times(0,T), \tag{2.7}$$

$$\boldsymbol{q}_i = \boldsymbol{q}_i^0 \text{ at } t = 0. \tag{2.8}$$

The first term on the right-hand-side has an effect of adjustment by which polarity $\boldsymbol{q}_i$ comes to meet $q_0^2 = |\boldsymbol{q}_i|^2$, where q_0 is decided arbitrarily. Chemotaxis is modeled by ∇c and $\boldsymbol{\zeta}_i$ represents a random number obtained under a stochastic distribution. Fictitious force is given as $\frac{d\boldsymbol{x}_i}{dt}$. Also, $\boldsymbol{q}_i^0$ is an initial condition of $\boldsymbol{q}_i$.

2.1.3. Field of fibronectin concentration

Finally, for real-valued parameters D, M, μ, a governing equation for a fibronectin concentration is defined as

$$\frac{df}{dt} = [\nabla \cdot M\nabla \{D\Delta f + w'\} - f\mu] H \text{ in } \Omega \times (0,T), \tag{2.9}$$

$$\boldsymbol{n} \cdot \nabla f = 0 \text{ on } \partial\Omega \times (0,T), \tag{2.10}$$

$$\boldsymbol{n} \cdot \nabla (D\Delta f + w') = 0 \text{ on } \partial\Omega \times (0,T), \tag{2.11}$$

$$f = f^0 \text{ at } t = 0, \tag{2.12}$$

where f^0 is an initial condition for f, and

$$H(\boldsymbol{x}, \boldsymbol{x}_i, t) = \sum_{i=1}^{N_{cell}} \exp\left(-\frac{|\boldsymbol{x} - \boldsymbol{x}_i|}{a_5}\right), \tag{2.13}$$

$$w'(f) = 2f(f-1)(2f-1). \tag{2.14}$$

3. Numerical scheme

Letting $t, \Delta t$ respectively stand for time and a time increment, then from discretizing the governing equation in the time direction at a time step $0 < n \leq N$ for $t = n\Delta t$, one can deduce

$$\frac{\boldsymbol{x}_i^{n+1} - \boldsymbol{x}_i^n}{\Delta t} = \varphi(f^n) \left\{ \hat{\boldsymbol{q}}_i^n + \sum_{j \neq i, j=1}^{N_{cell}} g_1 \frac{\boldsymbol{x}_j^n - \boldsymbol{x}_i^n}{r_{i,j}^n} \right\} - a_2 \nabla f^n, \tag{3.1}$$

$$\frac{\boldsymbol{q}_i^{n+1} - \boldsymbol{q}_i^n}{\Delta t} = M_q \left(q_0^2 - |\boldsymbol{q}_i^n|^2\right) \boldsymbol{q}_i^n + \nabla c + \boldsymbol{\zeta}_i^n + a_3 \frac{\boldsymbol{x}_i^{n+1} - \boldsymbol{x}_i^n}{\Delta t}, \tag{3.2}$$

$$H^{n+1} = \sum_{i=1}^{N_{cell}} \exp\left(-\frac{|\boldsymbol{x} - \boldsymbol{x}_i^{n+1}|}{a_5}\right), \tag{3.3}$$

$$\frac{f^{n+1} - f^n}{\Delta t} = \nabla \cdot \left[M\nabla \left\{D\Delta f^{n+1} + w'(f^n)\right\} - f^{n+1}\mu\right] H^{n+1}. \tag{3.4}$$

A random number $\boldsymbol{\zeta}_i^n$ is defined as

$$\boldsymbol{\zeta}_i^n = \boldsymbol{\zeta}_i^{n-1} - \alpha \boldsymbol{\zeta}_i^{n-1} + \boldsymbol{N}\sqrt{\Delta t}, \tag{3.5}$$

and $\boldsymbol{N} \in \mathbb{R}^d$ is a vector-valued function. A standard distribution with mean 0 and variance 1 is set at every element. All numerical simulations are performed by Freefem++ [26]. Especially, a fibronectin concentration is governed by the fourth-order partial differential equation. This paper using Morley element implemented in Freefem++ [26] to calculation the weak form of the Cahn–Hilliard equation.

4. Numerical result

A domain Ω is defined as

$$\Omega = \left\{\boldsymbol{x} = [x, y]^{\mathrm{T}}; 0 \leq x \leq 50, -25 \leq y \leq 25\right\}. \tag{4.1}$$

4.1. Basic features of the model

Before applying and assessing our suggested mathematical model, we confirm basic features of the model for particle collision and chemotaxis. For all cases, 10 particles are prepared initially. The position vector $\boldsymbol{x}_i$ and polarity $\boldsymbol{q}_i$ of each cell are expressed as

$$\boldsymbol{x}_i = [25 + N(0,1), N(0,1)], \tag{4.2}$$

$$\boldsymbol{q}_i = [N(0,1), N(0,1)], \tag{4.3}$$

where all the parameters are listed in Table 1.

Table 1. Parameters.

Symbol	Parameter	Value
a_1	Cell mobility	10
a_2	Repulsive force between cells and fibronectin	1
a_3	Chemotaxis to VEGF concentration	1
a_4	Cell alignment effect	0.1
a_5	Radius of influence of cells	0.1
D	Square of transition area width of fibronectin phase variable	1
M	Mobility of fibronectin regions	1
μ	Fibronectin Enzyme	1,10,100
q_0	Reference size of cell polarity	10
α	Persistence of cell polarity	0.1
d_{core}	Diameter of the cell (repulsive area)	12
$d_{neutral}$	Diameter of the cell (neutral area)	$1.5d_{core}$
d_{adh}	Diameter of the cell (adhesive area)	$1.534d_{core}$
d_{reach}	Diameter of the cell (interactable area)	$1.834d_{core}$
F_{rep}	Intercellular repulsive force	5
F_{att}	Intercellular attraction force	1
Δt	Time increment	0.002

This paper is our first trial to simulate a dynamics of angiogenesis by coupling multi-agent model and phase-field model. Therefore, there is few of previous reserches, and we set most of arbitrary parameters in temporal and spatial scales. As a result, this numerical results might be helpful to understand a dynamics of angiogenesis qualitatively, not quantitatively.

4.1.1. Particle collision

For investigation of particle collisions, VEGF is ignored with $c = 0$. The interparticle distance $r_{i,j}$ is much less than $d_{core} = 12$ because of an initial position vector $\boldsymbol{x}_i = [25 + N(0,1), N(0,1)]$. Therefore all particles are mutually repulsive, with no effects of chemotaxis by $c = 0$. Figures 1 and 2 show f and H to visualize the time evolution of vessel development and cell behaviors. In the early stages of numerical calculations, effects of repulsive force are the spreading of all cells. Subsequently, such cells with no effect of chemotaxis move slowly and become distant in the radial direction.

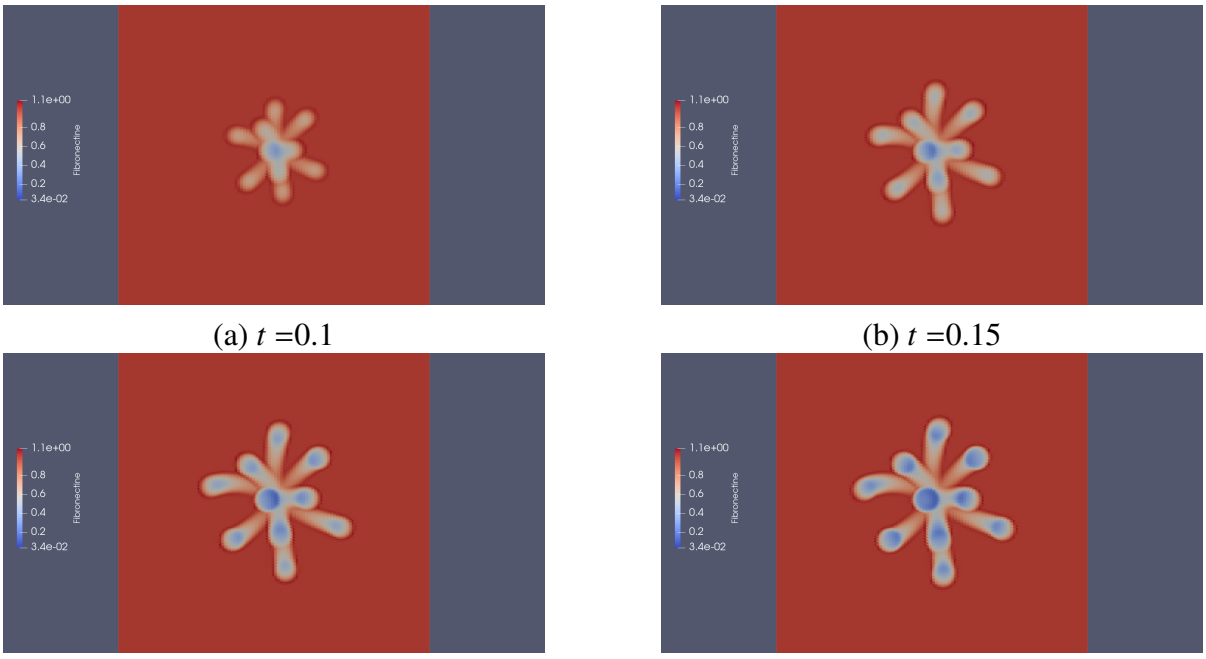

(a) t =0.1 (b) t =0.15

(c) t =0.2 (d) t =0.25

Figure 1. Time evolution of f without chemotaxis for $c = 0$.

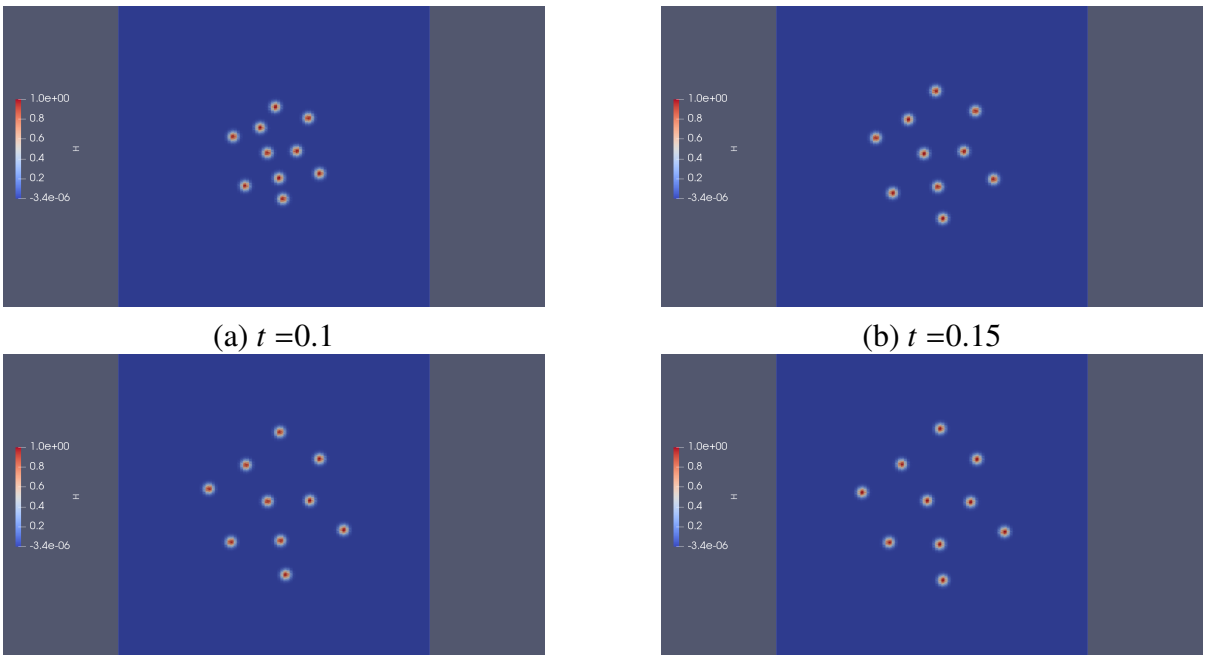

(a) t =0.1 (b) t =0.15

(c) t =0.2 (d) t =0.25

Figure 2. Time evolution of H without chemotaxis for $c = 0$.

4.1.2. Chemotaxis

Next, chemotaxis generated by VEGF is considered numerically with $c = 100x$. In the early stages of numerical calculations, effects of repulsive force are spreading of all cells, as discussed in the section above, because of stronger repulsive force than chemotaxis. Also, interparticle distance $r_{i,j}$ increases. After the repulsive force weakens sufficiently to become weaker than chemotaxis, all particles are moving in the right direction, where VEGF c has a larger value, as portrayed in Figures 3 and 4.

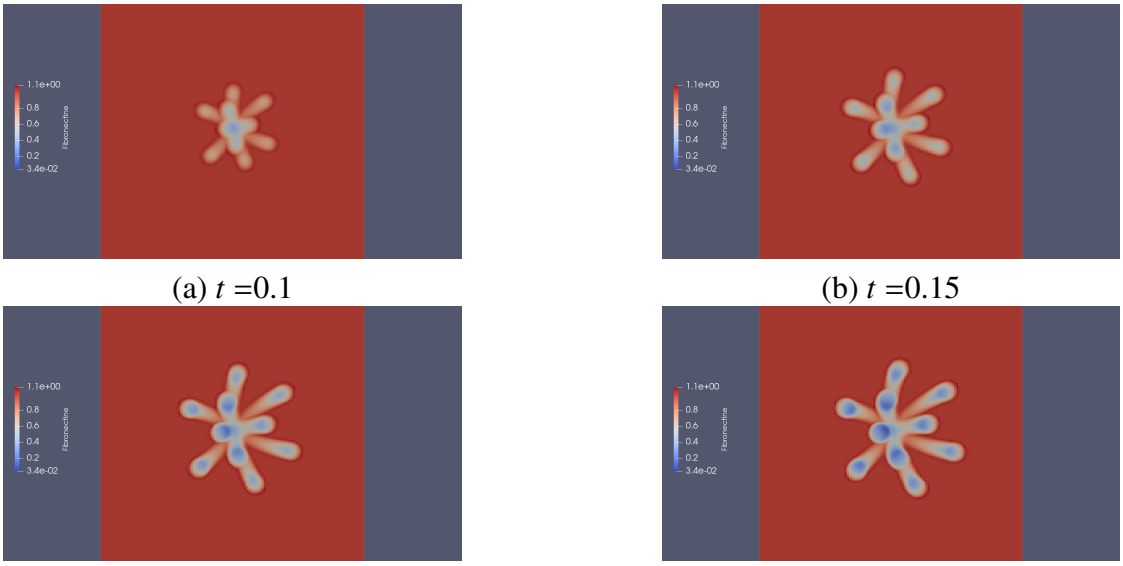

(a) t =0.1 (b) t =0.15

(c) t =0.2 (d) t =0.25

Figure 3. Time evolution of f with chemotaxis for $c = 100x$.

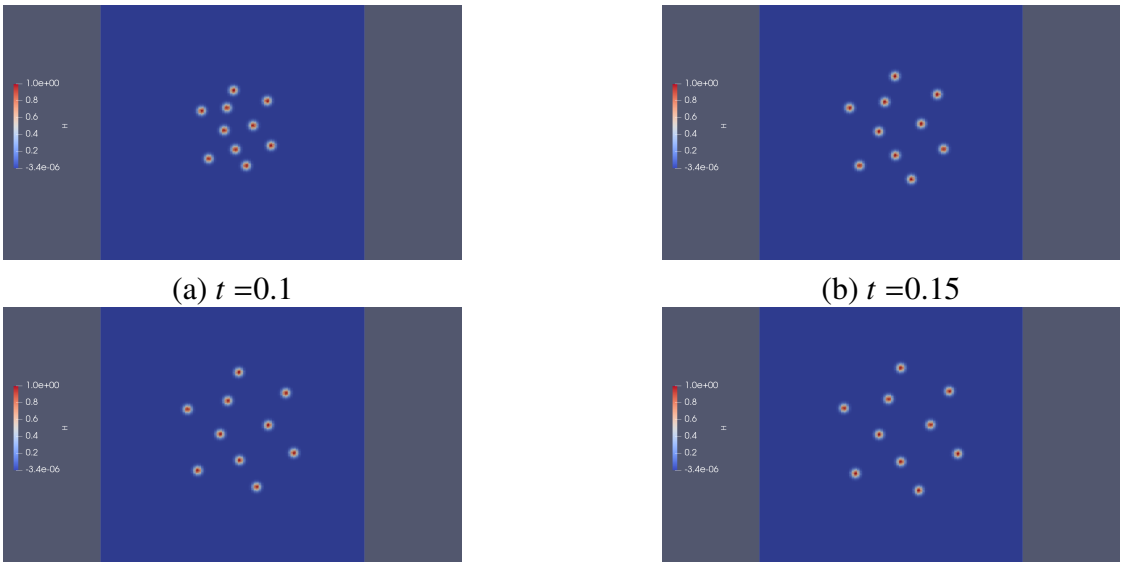

(a) t =0.1 (b) t =0.15

(c) t =0.2 (d) t =0.25

Figure 4. Time evolution of H with chemotaxis for $c = 100x$.

4.2. Numerical simulations of angiogenesis

Based on our suggested mathematical model and numerical techniques constructed in the sections presented above, we are performing numerical simulations not only of lateral inhibitation but also of elongation, branching, which are basic features of angiogenesis. The initial condition of position vector $\boldsymbol{x}_i$ and polarity $\boldsymbol{q}_i$ of each cell is expressed as

$$\boldsymbol{x}_i = [0.05 + N(0,1), N(0,1)], \tag{4.4}$$

$$\boldsymbol{q}_i = [1,0], \tag{4.5}$$

where the number of cells is 20. Then we set $x_i = 0.05$ in the case of $x_i < 0$; also, $c = 100x$ is used as VEGF. In fact, as a governing equation of fibronectin concentration f, the Cahn–Hilliard equation is representative of PDE models, but reduces to an ODE model by substituting $M = 0$. We calculate both to compare the results obtained from calculations.

Figure 5 portrays the time evolution of fibronectin f obtained in the case of ODE model with $M = 0$. The model has behavior of lateral inhibition and elongation, branching, and anastomosis. By contrast, Figure 6 portrays results obtained for the PDE model. The Cahn–Hilliard equation shows fibronectin f to be a distribution from 0 to 1. The structure of the vessel is therefore visualized as clearer than that of the ODE model. Next, we present Figure 7 in which the x coordinate of all cells is shown. As Figure 7 shows, all cells are moving quickly in the early stage because of mutual repulsion. Thereafter, chemotaxis ∇c attracts them to move slowly in the positive-x direction. Figure 8 presents data for comparison, illustrating differences of the same particles between the ODE model and PDE model. Some particles are observed to move with very different behaviors because of the effects of distribution of fibronectin f attributable to the distribution of the fibronectin concentration f in the ODE model, which differs from that of the PDE model.

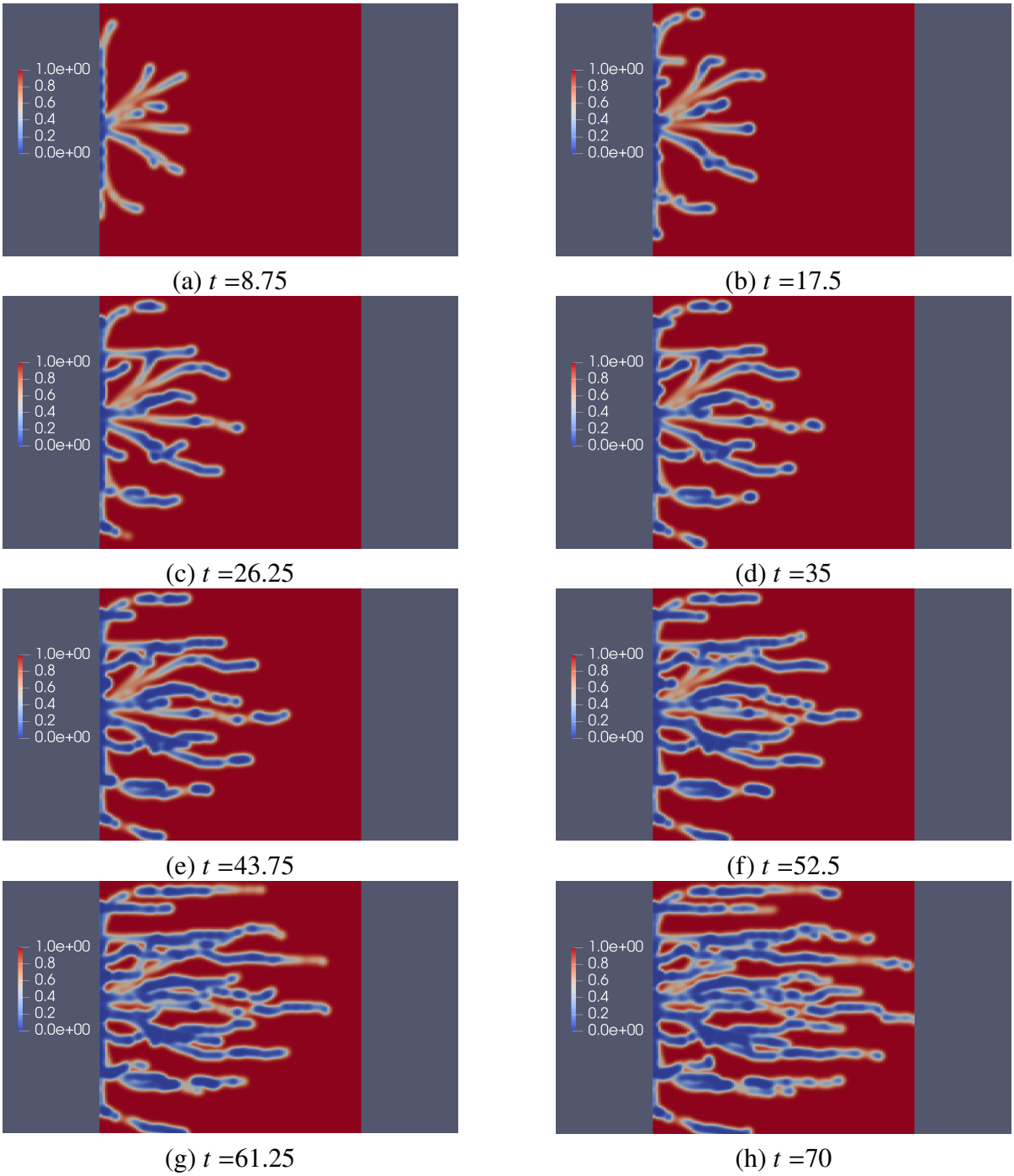

(a) t =8.75 (b) t =17.5

(c) t =26.25 (d) t =35

(e) t =43.75 (f) t =52.5

(g) t =61.25 (h) t =70

Figure 5. Time evolution of f with chemotaxis in the case of $c = 100x$ for the ODE model.

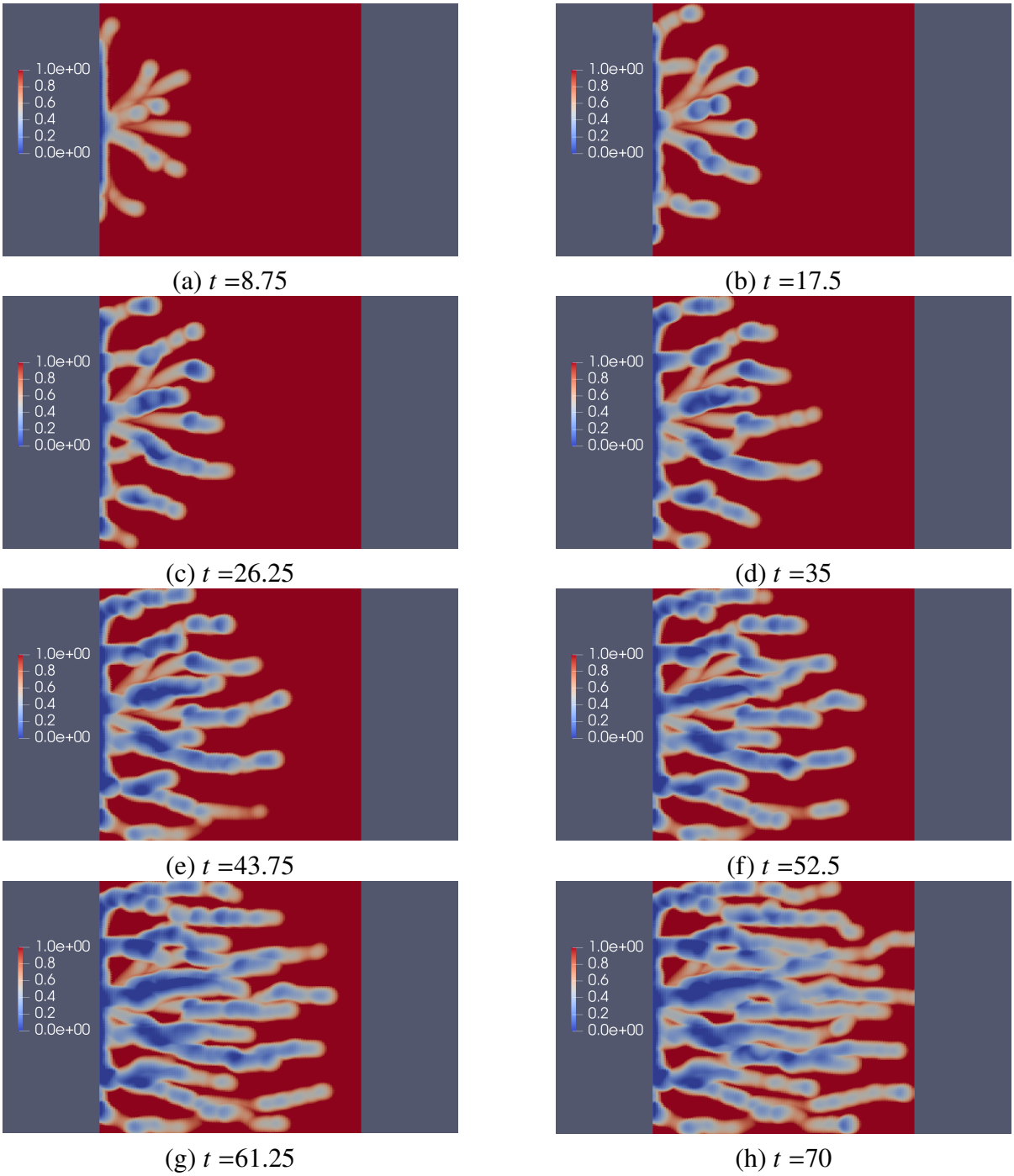

(a) t =8.75 (b) t =17.5

(c) t =26.25 (d) t =35

(e) t =43.75 (f) t =52.5

(g) t =61.25 (h) t =70

Figure 6. Time evolution of f with chemotaxis for $c = 100x$ for the PDE model.

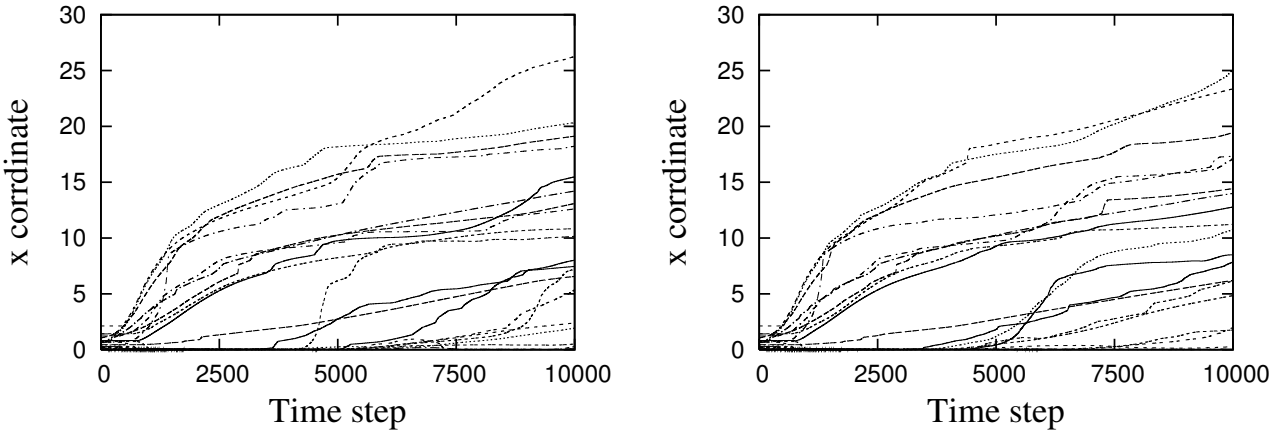

(a) $M = 0$ (b) $M = 1$

Figure 7. x coordinates of all cells with time steps up to $t = 20$.

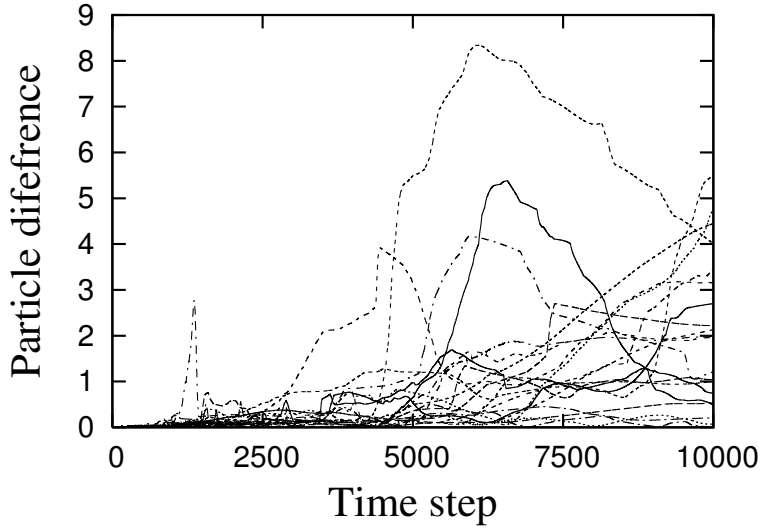

Figure 8. Particle difference between $M = 0$ and $M = 1$.

4.3. Attraction of vessels by tumor cells

Finally, on the assumption that tumor cells express vascular endothelial growth factor receptors and respond to autocrine and paracrine VEGF signals, this section defines VEFG as

$$c = 1000 \exp\left[-0.001\left\{(x-50)^2 + y^2\right\}\right], \tag{4.6}$$

where Figure 9 depicts the distribution of this c. An initial condition of position vector $\boldsymbol{x}_i$ and polarity $\boldsymbol{q}_i$ of each cell is expressed as

$$\boldsymbol{x}_i = [0.05 + N(0,1), N(0,6)], \tag{4.7}$$

$$\boldsymbol{q}_i = [1,0], \tag{4.8}$$

where the number of cells is 20. We set $x_i = 0.05$ in the case of $x_i < 0$. By the way, $N(0,1)$ is used in section 4.1 and 4.2. In the case of $N(0,1)$, it is seemed that effects of cross-interaction between particles themselves are strong in eraly stage. Thereofre, we set $N(0,6)$ in section 4.3 to focus on effects of a tumor cell.

Figure 10 shows the time evolution of f with chemotaxis at $t = 62$, unlike in the case of Figures 5 and 6, not all particles are moving in the x-direction. They coming in the direction of a coordinate $(x,y) = (50,0)$ with a maximum value of c. However, apparently, some particles are going to the lower right. Therefore we are concerned that this phenomenon is attributable to cell adhesion effects. The domain used for this simulation is 50×50 square. The cell diameter is $d_{adh} \approx 18$ from Table 1. Therefore, the top position cell affected by VEGF is moving in the lower right. Subsequent cells are following the top position cell because of cell adhesion.

Next, we observe vessel development depending on μ representing the strength for degenerating fibronectin and its corresponding x coordinate at each cell in the case of the PDE model. As presented in Figures 11–13, a small μ as in Figure 11 with $\mu = 1$ can suppress vessel development more than that shown in Figure 13 with $\mu = 100$ because a cell can be moving much more in the area of fibronectin $f = 0$ than $f = 1$. Consequently, numerical simulations of Figures 11–13 represent biochemically adequate numerical results.

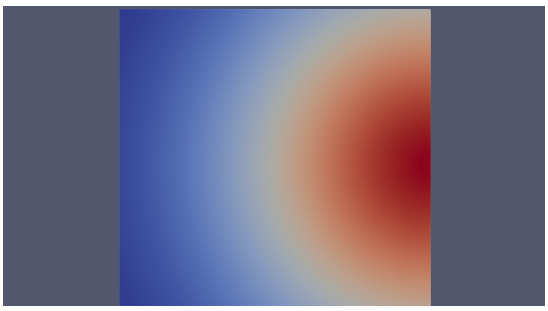

Figure 9. Distribution of c.

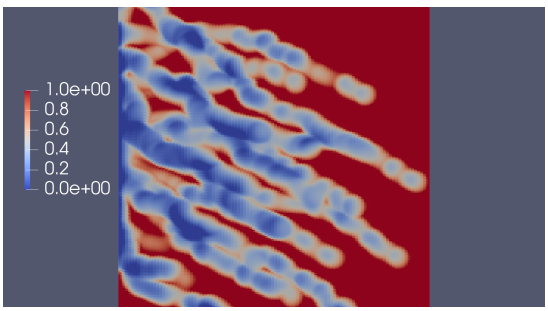

Figure 10. Time evolution of f.

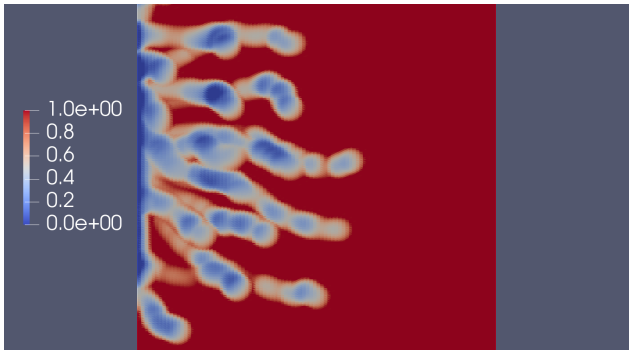

(a)

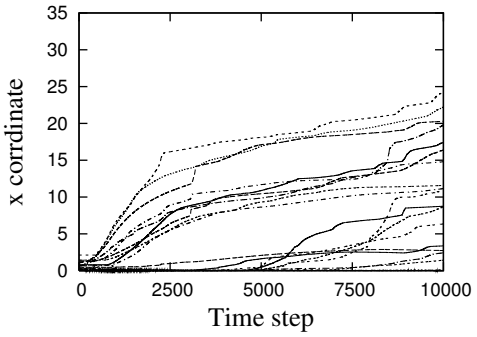

(b)

Figure 11. (a) Fibronectin f at $t = 30$ and (b) x coordinate at each cells up to t=20 for $\mu = 1$.

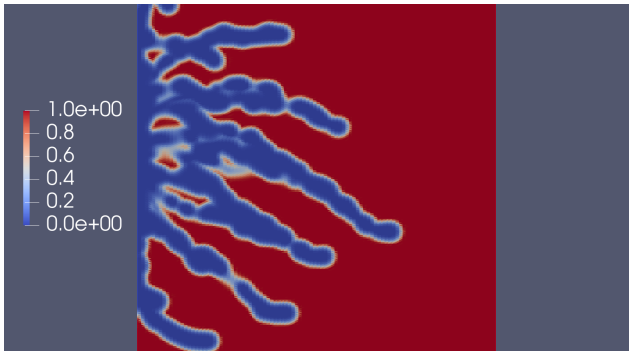

(a)

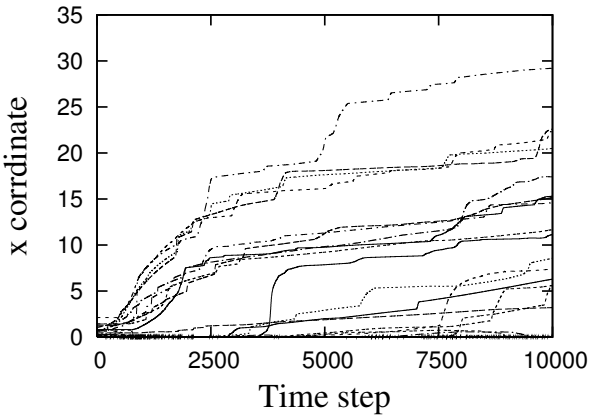

(b)

Figure 12. (a) Fibronectin f at $t = 30$ and (b) x coordinate at each cells up to t=20 for $\mu = 10$.

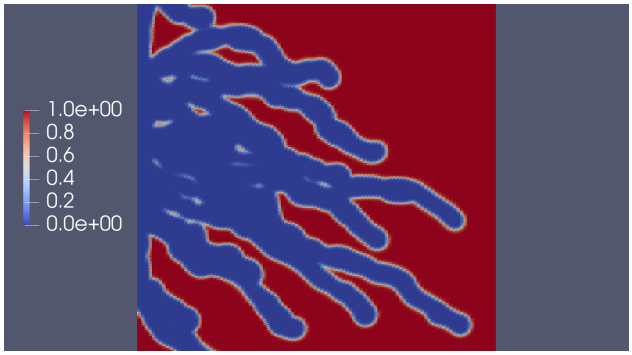

(a)

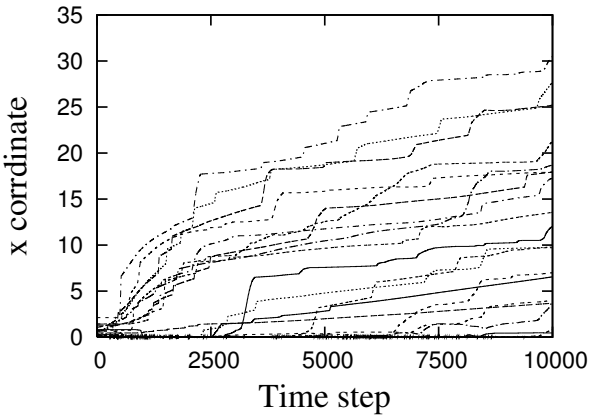

(b)

Figure 13. (a) Fibronectin f at $t = 30$ and (b) x coordinate at each cells up to t=20 for $\mu = 100$.

5. Conclusion

We demonstrated the characteristic features of angiogenic endothelial cell (EC) behaviors. Taken together with findings reported from earlier studies using experimentation such as that reported by Arima et al. [18], we suggest a multi-agent model coupled with phase-field model for angiogenic morphogenesis. Such a model enables us to dissect cellular mechanisms regulating dynamic and complex multicellular processes systematically. The Cahn–Hilliard equation is regarded as phase-field model, and ODE and PDE equation are prepared by switching $M = 0, 1$.

Our first numerical result is that multi-agent based EC movements with ODE model, represented as a process driven by a simple stochastic rule in this suggested multi-agent model, can adequately describe branch elongation, which plays an important role as one angiogenic model. However, EC behaviors were insufficiently explained using cell processes alone because the ODE model was not able to consider an effect of elasticity of a vessel wall. This numerical result leads to our second result suggesting that PDE model might be necessary for degenerating fibronectin f in the whole cell. This prediction was verified biologically. Consequently, this study advances our mathematical understanding of angiogenic morphogenesis as coordinated multicellular processes.

As described herein, a smaller area is adopted to suppress calculation cost to the greatest degree possible. Effects of cell adhesion are increased as result. It is too difficult to survey some biochemical phenomena precisely. Future work must be done for numerical calculation with a larger area than this study to investigate additional details about relations with chemotaxis ∇c and enzyme of fibronectin μ.

In fact, we need to analyze correlation between chemotaxis and heterogeneous directionality, cell mixing, cell overtaking, branching morphogenesis. However, it is seemed that effects of chemotaxis is much stronger than that of them, and we did not observe about details of the movement of ECs from our numerical simulation.

In the future, a multi cellular model suggested here will be quantitatively leading a life science reserch on molecular level and a cellular level to acquisitions of a macroscopic histogenesis and a vital function.

Acknowledgments

This work was supported by JSPS KAKENHI, Grant Number 19K03645, and MEXT KAKENHI, Grant Number 17H06327.

Conflict of interest

The authors declare no conflicts of interest in this paper.

References

1. Holderfield MT and Hughes CC (2008) Crosstalk between vascular endothelial growth factor, notch, and transforming growth factor-beta in vascular morphogenesis. *Circ Res* 102: 637–652. https://doi.org/10.1161/CIRCRESAHA.107.167171

2. De Smet F, Segura I, De Bock K, et al. (2009) Mechanics of vessels branching: filopodia on endothelial tip cells lead the way. *Arterioscle Thromb Vasc Biol* 29: 639–649. https://doi.org/10.1161/ATVBAHA.109.185165

3. Armulik A, Abramsson A, Betsholtz C (2005) Endothelial/pericyte interactions. *Circ Res* 97: 512–523. https://doi.org/10.1161/01.RES.0000182903.16652.d7

4. Gaengel K, Genove G, Armulik A, et al. (2009) Endothelial-mural cell signaling in vascular development and angiogenesis. *Arterioscle Thromb Vasc Biol* 29: 630–638. https://doi.org/10.1161/ATVBAHA.107.161521

5. Hellstrom M, Gerhardt H, Kalen M, et al. (2001) Lack of pericytes engenders endothelial hyperplasia and abnormal vascular morphogenesis. *J Cell Biol* 153: 543–554. https://doi.org/10.1083/jcb.153.3.543

6. Lafleur MA, Forsyth PA, Atkinson SJ, et al. (2001) Perivascular cells regulate endothelial membrane type-1 matrix metalloprotainase activity. *Biochem Biophy Res* 282: 463–473. https://doi.org/10.1006/bbrc.2001.4596

7. Liu H, Kennard S, Lilly B (2009) NOTCH3 expression is induced in mural cells through an autoregulatory loop that requires endothelial-expressed JAGGED1. *Circ Res* 104: 466–475. https://doi.org/10.1161/CIRCRESAHA.108.184846

8. Frieboes HB, Lowengrub JS, Wise SM, et al. (2007) Computer simulation of glioma and morphology. *Neuroimage* 37: 59–70. https://doi.org/10.1016/j.neuroimage.2007.03.008

9. Wise SM, Lowengrub JS, Frieboes HB, et al. (2008) Three-dimensional multispecies nonlinear tumor growth – 1: Model and numerical method. *J Theor Biol* 253: 524–543. https://doi.org/10.1016/j.jtbi.2008.03.027

10. Frieboes HB, Jin F, Chuang YL, et al. (2010) Three-dimensional multispecies nonlinear tumor growth – 2: tumor invasion and angiogenesis. *Neuroimage* 264: 1254–1278. https://doi.org/10.1016/j.jtbi.2010.02.036

11. Lima EA, Oden JT, Almeida RC (2014) A hybrid ten-species phase-field model of tumor growth. *Math Models Methods Appl Sci* 24: 2569–2599. https://doi.org/10.1142/S0218202514500304

12. Perfahl H, Bryne HM, Chen T, et al. (2011) Multiscale modelling of vascular tumor growth in 3D: The role of domain size and boundary conditions. *PloS One* 6: e14790. https://doi.org/10.1371/journal.pone.0014790

13. Alber MS, Kiskowski MA, Glazierz JA, et al. (2003) On cellular automaton approaches to modelling biological cells, In: Rosenthal J, Gilliam DS, *Mathematical Systems Theory in Biology, Communications, Computation, and Finance*, New York: Springer, 1–39. https://doi.org/10.1007/978-0-387-21696-6_1

14. McAneney H and O'Rourke SFC (2007) Investigation of various growth mechanisms of solid tumor growth within the linear-quadratic model for radiotherapy. *Phys Med Biol* 52: 1039–1054. https://doi.org/10.1088/0031-9155/52/4/012

15. Rejniak KA and Anderson ARA (2010) Hybrid models of tumor growth. *Wires SystBiol Med* 3: 115–125. https://doi.org/10.1002/wsbm.102

16. Boondirek A and Lenbury Y (2006) A stochastic model of cancer growth with immune response. *J Kor Phy Phys Soc* 4: 1652–1666.
17. Gerlee P and Anderson ARA (2008) A hybrid cellular automaton model of clonal evolution in cancer: The emergence of the glycolytic phenotype. *J Thero Biol* 250: 705–722. https://doi.org/10.1016/j.jtbi.2007.10.038
18. Arima S, Nishiyama K, Ko T, et al. (2011) Angeogenesis morphogenesis driven by dynamic and heterogeneous collective endothelial cell movement. *Development* 138: 4763–4776. https://doi.org/10.1242/dev.068023
19. Takubo N, Yura F, Naemura K, et al. (2019) Cohesive and anisotropic vascular endotherial cell motility driving angiogenic morphogenesis. *Scientific Reports* 9: 9034. https://doi.org/10.1038/s41598-019-45666-2
20. Cahn JW and Hilliard JE (1958) Free energy of a nonuniform system. I. Interfacial free generic interface. *J Chem Phys* 28: 258–267. https://doi.org/10.1063/1.1744102
21. Furihata D and Matsuo T (2011) *Discrete Variational Derivative Method: A structure-preserving numerical method for partial differential equations*, Nwe York: CRC Press. https://doi.org/10.1201/b10387
22. Feng X, Li Y, Xing Y (2016) Analysis of mixed interior penalty discontinuous Galerkin methods for the Cahn–Hilliard equation and the Hele–Shaw flow. *SIAM J Numer Anal* 54: 825–847. https://doi.org/10.1137/15M1009962
23. Kovacs M, Larsson S, Mesforsh A (2011) Finite element approximation of the Cahn–Hilliard–Cook equation. *SIAM J Numer Anal* 49: 2407–2429. https://doi.org/10.1137/110828150
24. Brenner SC, Sung Li-y, Zhang H, et al. (2013) A Morley finite element method for the displacement obstacle problem of clamped Kirchhoff plate. *J Comp Appl Math* 254: 31–42. https://doi.org/10.1016/j.cam.2013.02.028
25. Li M, Guan X, Mao S (2014) New error estimates of the Morley element for the plate bending problems. *J Comp Appl Math* 263: 405–416. https://doi.org/10.1016/j.cam.2013.12.024
26. Hecht F (2012) New development in FreeFem++. *J Numerical Math* 20: 251–266. https://doi.org/10.1515/jnum-2012-0013
27. Sánchez-Pérez R, Pavan S, Mazzeo R, et al. (2018) Mutation of a bHLH transcription factor allowed almond domestication. *Science* 364: 1095–1098. https://doi.org/10.1126/science.aav8197

AIMS Press